# Supporting information

# Ag incorporation in atomically precise $Au_3Ag_3Cu_6$ nanoclusters promotes electrocatalytic nitrate-to-ammonia conversion

Liwen Li,[≠,a] Anqi Xie, [≠,a] Cao Fang,[a] Lin Xiong,[*,b] Yingqiang Sun,[*,a] Shan Jin,[*,a] and Manzhou Zhu[a]

[a] Key Laboratory of Structure and Functional Regulation of Hybrid Materials of Ministry of Education, Institutes of Physical Science and Information Technology, Department of Materials Science and Engineering, Centre for Atomic Engineering of Advanced Materials, Anhui University, Hefei 230601, China. Emails: jinshan@ahu.edu.cn, syq38@mail.ustc.edu.cn
[b] School of Food and Chemical Engineering, Shaoyang University, Shaoyang 422000, PR China. Email: linxiong@hnsyu.edu.cn
≠They contributed equally to this work.

## Materials and Reagents

Copper tetrafluoroborate tetracyanide ($[Cu(CH_3CN)_4]BF_4$, 98%), $HAuCl_4·3H_2O$ (99% metal basis), silver nitrate ($AgNO_3$, 99%), 3,5-bis(trifluoromethyl)benzenethiol (SR, 98%), sodium borohydride ($NaBH_4$, 99%), and 2,6-bis(diphenylphosphino)pyridine (dpppy, 98%), dichloromethane (DCM, HPLC grade), methanol (MeOH, HPLC grade), ethyl alcohol (EtOH HPLC grade), acetone (ACE, HPLC grade), and *n*-hexane (*n*-Hex, HPLC grade).

## Synthesis of the $Au_3Cu_9(SR)_6(dpppy)_3Cl_5$ nanocluster

In a 50 mL round-bottom flask, dissolve 60 mg of $[Cu(CH_3CN)_4]BF_4$ and 40 mg of $HAuCl_4·3H_2O$ in 10 mL of ACE and 10 mL of DCM. Stir the solution vigorously at room temperature for 10 minutes; the solution immediately turns green. Next, add 100 mg of 2,6-bis(diphenylphosphine)pyridine to the flask. After reacting for 5 minutes, add 50 μL of 3,5-bis(trifluoromethyl)benzenethiol under vigorous stirring, and the solution turns orange. Then, 1 mL of sodium borohydride methanol solution (10 mg $mL^{-1}$) is rapidly added to the reaction mixture under vigorous stirring, and the solution color immediately changes from orange to brown. The reaction is then carried out at room temperature for 5 houSR until the solution turns yellow, indicating the formation of the cluster. The mixture is then washed three times with DCM and *n*-hex. The crystal was crystallized in DCM/*n*-hex (1:3) under dark conditions at room temperature, and orange needle-like single crystal were obtained after 3 days. Based on the Au element used for synthesizing the $Au_3Cu_9$ nanocluster (calculated from $HAuCl_4·3H_2O$), the yield is 29%.

## Synthesis of the $Au_3Ag_3Cu_6(SR)_6(dpppy)_3Cl_5$ nanocluster

The method for synthesizing $Au_3Ag_3Cu_6$ is essentially the same as that for $Au_3Cu_9$, except that after adding 1 mL of sodium borohydride methanol solution (10 mg $mL^{-1}$), 60 mg of $AgNO_3$ is added, causing the solution color to change from brown to black. The washing method remains the same, and after 5 days, orange-yellow rod-shaped single crystals are obtained. Based on the Au element used for

synthesizing $Au_3Ag_3Cu_6$ nanoclusters (calculated from $HAuCl_4 \cdot 3H_2O$), the yield is 36%.

# Experimental method

## Characterizations

Electrospray ionization mass spectrometry (ESI-MS) was conducted on a Waters XEVO G2-XS QT mass spectrometer. Thermogravimetric analysis (TGA) was performed using a Shimadzu DTG-60H instrument. Powder X-ray diffraction (PXRD) data were collected on a Rigaku Smartlab 9 kW diffractometer equipped with a Cu Kα radiation source operating at 40 kV and 200 mA, with a scanning range of 2θ = 10 - 80° and a step size of 0.01°. X-ray photoelectron spectroscopy (XPS) measurements were carried out on a Thermo ESCALAB 250 spectrometer using a monochromated Al Kα X-ray source (1486.8 eV) at 150 W with a spot size of 0.5 mm. The analysis chamber was maintained at a base pressure better than $1\times10^{-9}$ mbar, and spectra were recorded with a pass energy of 20 eV. Ultraviolet-visible (UV-vis) absorption spectra of all nanoclusters were obtained using an Agilent 8453 spectrophotometer. Photoluminescence (PL) spectra were measured with a HORIBA Fluoro Max$^+$ spectrofluorometer, and fluorescence lifetimes were determined on a HORIBA FluoroMax-4P instrument using diluted solutions. Single-crystal X-ray diffraction (SC-XRD) data were acquired on a Stoe Stadivari diffractometer under a nitrogen stream at 120 K, employing graphite-monochromated Cu Kα radiation (λ = 1.54186 Å). Data reduction was performed using the SAINT software, and structural refinement was conducted with Olex 2.

## Electrochemical measurements

The electrocatalytic reduction of nitrate was conducted using a CHI 660E electrochemical workstation. A three-electrode configuration was employed, with nickel foam-supported cluster catalysts serving as the working electrode, platinum sheets functioning as the counter electrode, and Ag/AgCl electrodes acting as the reference electrode. The reaction took place in an H-shaped electrolytic cell at room temperature, with the anode and cathode chambers physically separated by Nafion 117 membranes. The specific preparation process of the working electrode is as follows: Firstly, 5 mg of cluster solid is weighed and mixed with 480 μL of deionized water, 480 μL of anhydrous ethanol and 40 μL of Nafion solution with a mass fraction of 5%. After ultrasonic dispersion treatment, a uniform and orange-yellow ink is obtained. Subsequently, 40 μL of ink was taken with a pipette and evenly coated on the surface of a pre-cut 1 cm × 1 cm nickel foam in five equal portions, and let it dry naturally at ambient temperature to form the final catalytic electrode. In the electrochemical test, 40 mL of 0.5 M $K_2SO_4$ electrolyte containing 0.5 M $KNO_3$ was injected into the cathode chamber, while 40 mL of 0.5 M $K_2SO_4$ solution was used in the anode chamber. The electrochemical behavior of the electrode was investigated by linear scanning voltammetry. The scanning speed was fixed at 50 mV/s. All recorded current data were standardized based on the geometric area of the working electrode to be converted into current density. Before implementing potentiostatic electrolysis, linear scanning should be continuously carried out at this scanning rate until the obtained volt-ampere curve tends to be stable and has good repeatability. The final potentiostatic electrolysis experiment was carried out at different selected potentials respectively. The continuous reaction time at each potential point was 1 hour. During the experiment, the cathode electrolyte was continuously disturbed at a speed of 800 rpm by a magnetic stirrer to ensure effective mass transfer between the reactants and the electrode interface.

## Determination of products

The concentration of ammonium ions ($NH_4^+$) in the reaction solution was quantitatively analyzed using the indolephenol blue method. The specific steps are as follows: First, accurately measure 2 mL

of the reaction solution to be tested. Next, add 2 mL of a 1 M sodium hydroxide mixed solution containing 2 wt.% salicylic acid and 1 wt% sodium citrate. This addition facilitates the complexation reaction between salicylic acid and ammonium ions under alkaline conditions. Subsequently, 0.2 mL of the diluted 0.05 mol $L^{-1}$ sodium hypochlorite solution and 0.2 mL of the 1 wt.% sodium nitroprusside solution were combined. The resulting mixture was allowed to stand at room temperature for 2 hours to facilitate complete color development. Subsequently, the absorbance value of the absorption peak at 655 nm was measured using an ultraviolet-visible spectrophotometer. For quantitative analysis, standard curves were generated concurrently using ammonium chloride standard solutions at concentrations of 1 mg $L^{-1}$, 2 mg $L^{-1}$, 3 mg $L^{-1}$, 4 mg $L^{-1}$, and 5 mg $L^{-1}$. The concentration of $NH_4^+$ in the samples was determined by comparison with these standard curves.

The quantitative analysis of $NO_3^-$ concentration was conducted using ultraviolet spectrophotometry. Initially, the liquid sample obtained from the cathode chamber was diluted and pre-treated. It was then mixed with 100 μL of 1 M HCl and 10 μL of a 0.8 wt.% sulfamic acid solution, followed by dilution to a final volume of 5 mL with water. The solution was allowed to stand at room temperature for 20 minutes to ensure stability, after which its ultraviolet absorption spectrum was measured. The absorbance was corrected using the dual-wavelength calculation method of $A_{220nm}$ - $2A_{275nm}$ to effectively eliminate the background signal. This approach was calibrated with standard solutions of sodium nitrate at varying concentrations, facilitating accurate determination of the sample concentration.

The Gress test method was employed to quantitatively analyze $NO_2^-$ in the cathode electrolyte. Initially, the chromogenic reagent was prepared by dissolving 0.2 grams of N-(1-naphthyl) ethylenediamine dihydrochloride, 4 grams of sulfonamide, and 10 mL of phosphoric acid in 50 mL of deionized water. This mixture was thoroughly mixed and stored in the dark. For the measurement, an appropriate volume of the sample was reacted with 100 μL of the chromogenic reagent, followed by the addition of water to achieve a final volume of 5 mL. After a color development period of 20 minutes, a characteristic absorption peak was observed at 540 nm, with absorbance intensity being directly proportional to the $NO_2^-$ concentration. Accurate quantification was accomplished by comparison with the standard curve.

## Isotope labeling and $NH_4^+$ quantification by $^1H$ NMR analysis

For the detection of ammonium ions via $^1H$ NMR spectroscopy, the target solution (125 μL), maleic acid (15 mM, 125 μL), and sulfuric acid (50 μL) were mixed with deuterated dimethyl sulfoxide (DMSO-$d_6$, 750 μL). The mixed solution was analyzed using a $^1H$ NMR spectrometer (600 MHz), revealing two peaks corresponding to $^{15}NH_4^+$ and/or three peaks for $^{14}NH_4^+$, along with the peak of the internal standard maleic acid. For isotopic labeling, the electrolyte from the $K^{15}NO_3$ reaction after 1 hour of electrolysis was subjected to $^1H$ NMR analysis. The detection of two characteristic peaks for $^{15}NH_4^+$ confirmed that the nitrogen source of the synthesized ammonium ions originated entirely from the nitrate reactant[3].

## Formula for calculating Faraday efficiency, yield and removal rate.

The Faradaic efficiency was defined from the electric charge consumed for synthesizing ammonia and total charge passed through the electrode.

$$FE_{NH_3} = \frac{8 \times F \times c_{NH_3}}{Q} \times 100\% \#(1)$$

The yield was calculated using the following method：

$$Yield_{NH3} = \frac{c_{NH_3} \times V}{18 \times t \times S} \#(2)$$

The $FE_{NO_2^-}$ was calculated using the following method：

$$FE_{NO_2^-} = \frac{2 \times c_{NO_2^-} \times F \times V}{Q} \times 100\% \#(3)$$

The $NO_3^-$ removal rate was calculated using the following method：

$$NO_3^- removal\ rate = \frac{c_{\Delta N - NO_3^-}}{c_0} \#(4)$$

where $c_{NH3}$ and $c_{NO2}^-$ are the concentrations (mol $L^{-1}$) of $NH_3$ and $NO_2^-$ , $c_o$ represents the initial $NO_3^-$ concentration, $c_{\Delta N\text{-}NO3}^-$ represent the amount of $NO_3^-$ consumed before and after the reaction, respectively, as determined by UV-vis spectrophotometry, S is the geometric area of the working electrode (1 $cm^2$), t is the reaction time (1 h), F is the Faraday constant (96485 C $mol^{-1}$), V is the volume of electrolyte in the cathode compartment (40 mL), Q is the total charge consumed at the electrode.

**Calculation details**

The structural optimization and single-point energy of $Au_3Cu_9$ and $Au_3Ag_3Cu_6$ clusters are implemented using ORCA5.0.4 program system[1, 2] at the PBE0[3](D3BJ)/Def2-SVP[4] and PBE0[3](D3BJ)/Def2-TZVP[4] theoretical level, respectively. The basis sets of the Def2 series are equipped with relativistic pseudopotentials for elements after the fourth period, which can reflect the scalar relativistic effects. All free energy changes (Δ*G*) were computed using density functional theory (DFT) incorporating an implicit solvation model to account for aqueous solvent effects. The SMD implicit solution model was employed to simulate the water environment. Zero-point energy (ZPE) corrections and thermodynamic entropy contributions at 298.15 K, derived from vibrational frequency calculations (at the same level of theory as that used for geometry optimization), were included in all reported free energies. It should be noted that, in consideration of the high computational cost associated with vibrational frequency calculations, we simplified the R ligand. The Δ*G* was evaluated according to the following expression:

$$\Delta G = \Delta E + \Delta ZPE - T\Delta S \#(5)$$

Where Δ*E* is the change in reaction energy directly obtained from DFT total energies, Δ*ZPE*is the change in zero-point energy, *T* is the system temperature (298.15 K), and Δ*S* is the change in entropy. Both zero-point energies and entropies were derived from vibrational frequency calculations. For the $Au_3Cu_9$ and $Au_3Ag_3Cu_6$ clusters, all adsorbed species relevant to the reaction mechanism were fully optimized. Non-adsorbed species ($NH_3$, $H_2O$, and $H_2$) were analyzed using the same computational protocols as described for the adsorbed species. The reaction free energies of the electrochemical steps were evaluated using the computational hydrogen electrode (CHE) approach proposed by Nørskov et al., where the chemical potential of a proton-electron pair ($H^+ + e^-$) in solution is equated to half the chemical potential of gaseous $H_2$.[5, 6]

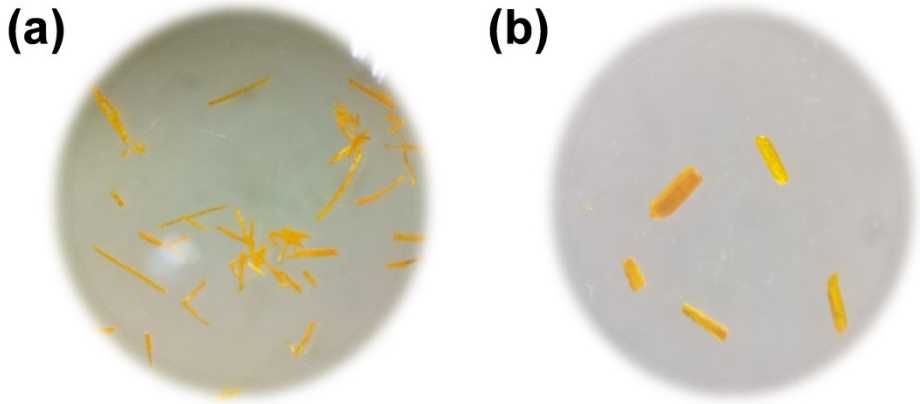


**Figure S1**. The single crystal photo of (a) $Au_3Cu_9$ and (b) $Au_3Ag_3Cu_6$ under microscope.

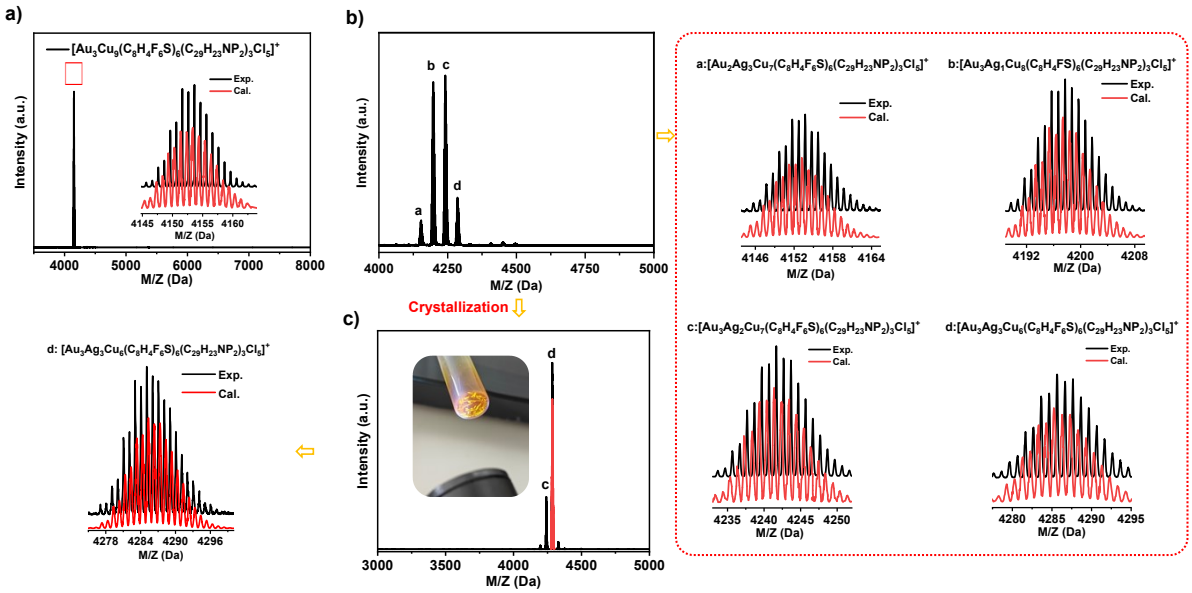


**Figure S2.** The ESI-MS results of (a) $Au_3Cu_9$, (b) crude sample of the trimetallic including $Au_3Ag_3Cu_6$ NCs and (c) final cluster $Au_3Ag_3Cu_6$ isolated by crystallization.

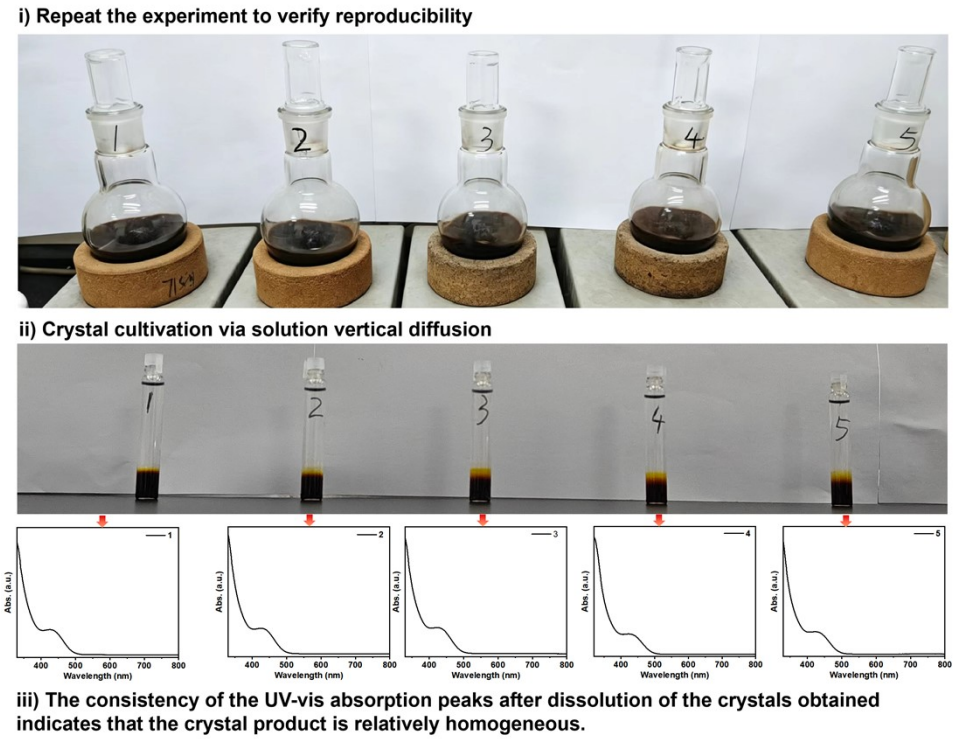


**Figure S3**. The repeated synthesis preparation, crystal growth, and UV-visible spectral characterization experiments of $Au_3Ag_3Cu_6$.

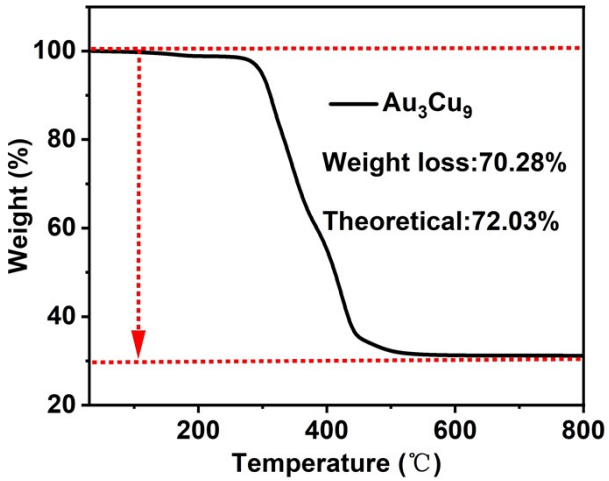


**Figure S4.** The TGA curves of $Au_3Cu_9$ in $N_2$ atmosphere.

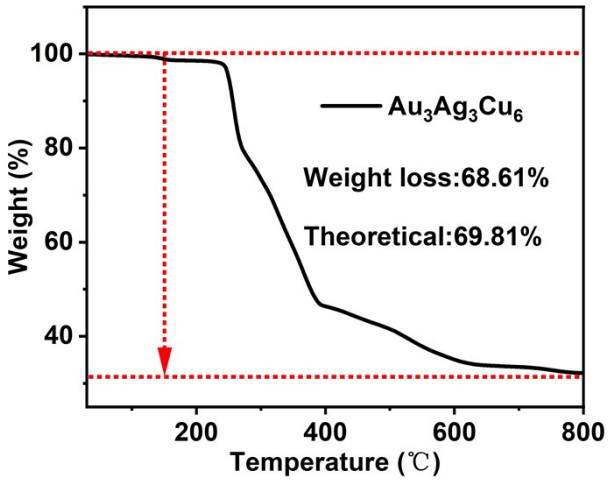


**Figure S5.** The TGA curves of $Au_3Ag_3Cu_6$ in $N_2$ atmosphere.

Thermogravimetric analysis (TGA) was performed to evaluate the thermal stability and ligand composition of $Au_3Cu_9$ and $Au_3Ag_3Cu_6$ nanoclusters. The theoretical weight loss was calculated based on the precise molecular formula confirmed by single-crystal XRD and ESI-MS. Briefly, the total molecular weight of all surface ligands (including thiolate, dpppy phosphine and chloride ions) was divided by the overall molecular weight of the intact nanocluster to obtain the theoretical ligand loss ratio, and the residual mass at high temperature corresponds to the inorganic metal core.

The $Au_3Cu_9$ nanocluster exhibits three successive weight-loss stages: the slight mass loss within 30-200 °C is attributed to the removal of adsorbed organic solvents and physical water; the obvious weight loss at 200-380 °C originates from the detachment and decomposition of thiolate ligands and partial chloride ions; the continuous decay at 450-600 °C is assigned to the complete degradation of phosphine ligands and residual chloride, finally forming stable metal alloy residues.

In comparison, $Au_3Ag_3Cu_6$ displays four distinct thermal decomposition steps, involving solvent desorption at low temperature, early decomposition of partial thiol ligands, intensive degradation of major organic ligands, and thorough removal of residual ligands accompanied by metal core stabilization at high temperature. The different TGA behaviors of the two nanoclusters stem from the introduction of Ag atoms, which modulates the metal-ligand coordination interaction and electronic distribution of the trimetallic core, thereby altering the thermal stability and sequential dissociation behavior of surface ligands. For both samples, the experimental total weight loss matches well with the theoretical calculation result, further demonstrating the high phase purity and compositional uniformity of the synthesized nanoclusters.

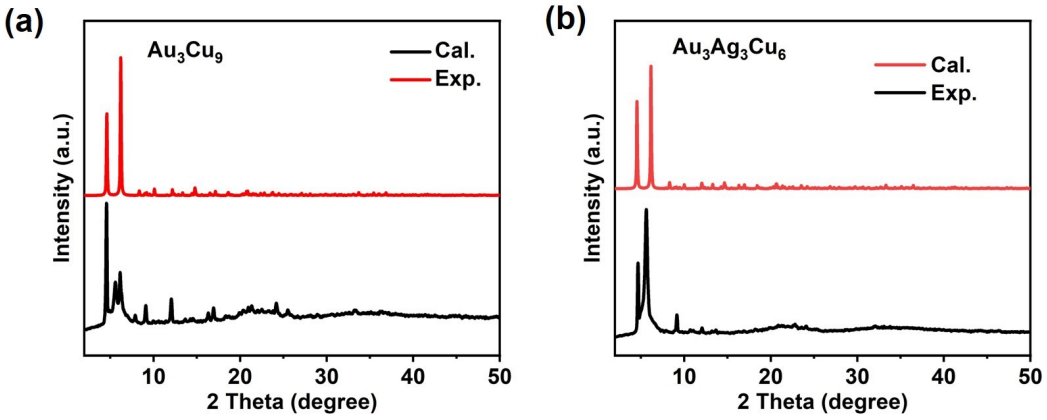


**Figure S6.** XRD patterns of (a) $Au_3Cu_9$ and (b) $Au_3Ag_3Cu_6$.

Both $Au_3Cu_9$ and $Au_3Ag_3Cu_6$ display well-defined, sharp diffraction peaks that closely match the simulated patterns derived from single-crystal XRD data. Moreover, the collected diffraction peaks present accurate positions, uniform relative intensities and negligible peak broadening or splitting, strongly demonstrating the single-phase nature and high crystallinity of the two samples. Collectively, the PXRD results verify the high phase purity and structural homogeneity of the as-prepared atomically precise nanoclusters.

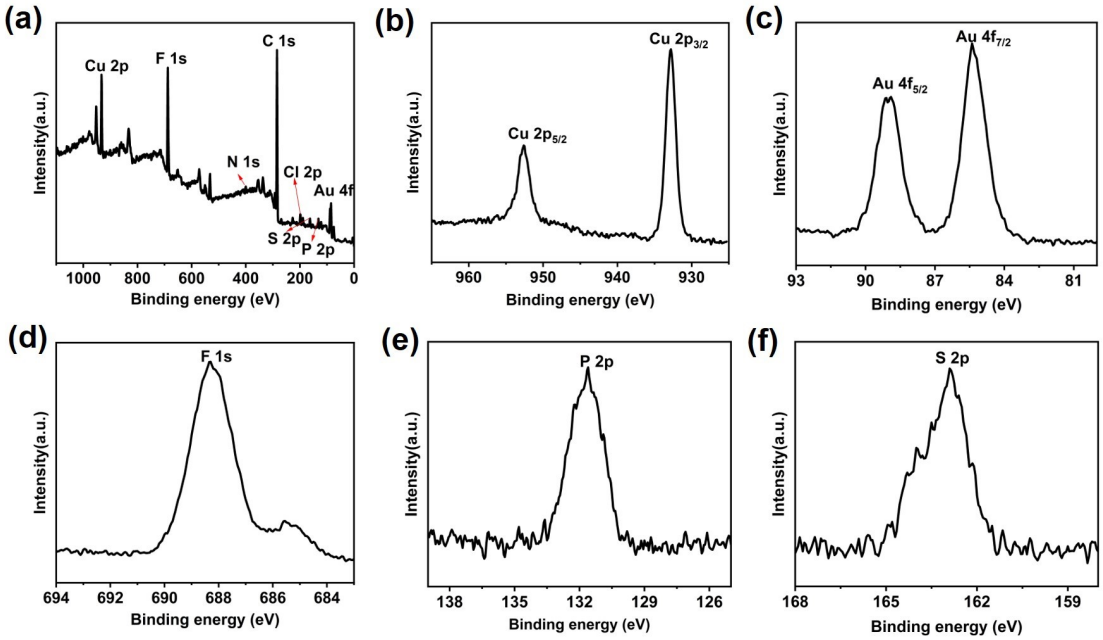


**Figure S7.** The XPS survey of (a) $Au_3Cu_9$. The High-resolution XPS spectra of (b) Cu, (c) Au, (d) F, (e) S, (f) P of $Au_3Cu_9$.

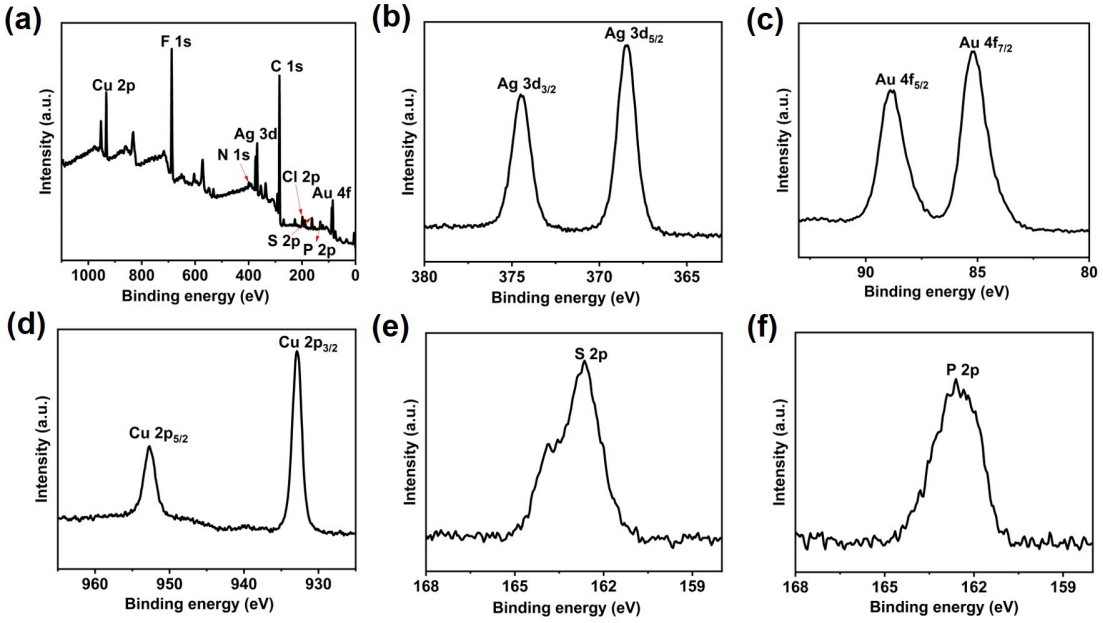


**Figure S8.** The XPS survey of (a) $Au_3Ag_3Cu_6$. The High-resolution XPS spectra of (b) Cu, (c) Au, (d) F, (e) S, (f) P of $Au_3Ag_3Cu_6$.

For the $Au_3Cu_9$ sample, the Au $4f_{7/2}$ and Au $4f_{5/2}$ peaks located at 85.40 eV and 88.90 eV verify the monovalent state of Au, while the Cu $2p_{3/2}$ and Cu $2p_{1/2}$ signals at 932.80 eV and 952.60 eV confirm

the Cu(I) configuration. In comparison, $Au_3Ag_3Cu_6$ exhibits nearly identical Au and Cu binding energies, demonstrating the retention of Au(I) and Cu(I) valence states. The characteristic Ag $3d_{5/2}$ and Ag $3d_{3/2}$ peaks at 368.39 eV and 374.50 eV further prove that Ag exists mainly in the form of Ag(I) within the trimetallic nanocluster.

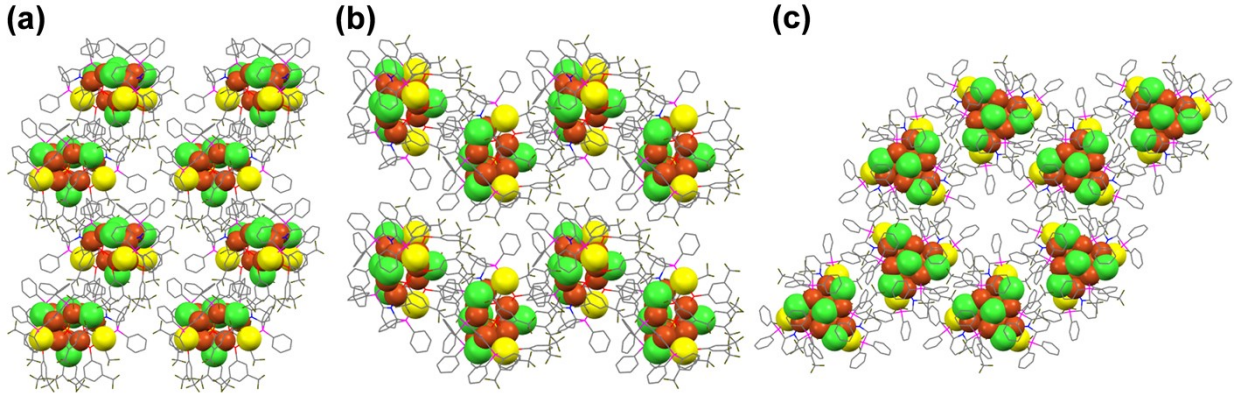


**Figure S9.** The packing diagram of $Au_3Cu_9$. View from (a) a direction, (b) b direction, and (c) c direction. Atom colors: yellow, Au; orange Cu; red, S; magenta, P; or green, F; gray, C. All hydrogen atoms are omitted for clarity.

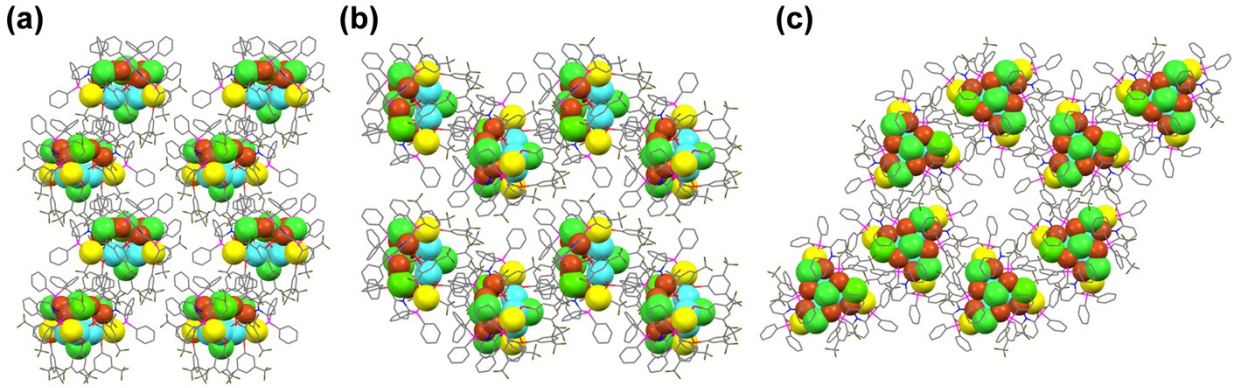


**Figure S10.** The packing diagram of $Au_3Ag_3Cu_6$. View from (a) a direction, (b) b direction, and (c) c direction. Atom colors: yellow, Au; sky blue, Ag; red, S; magenta, P; or green, F; gray, C. All hydrogen atoms are omitted for clarity.

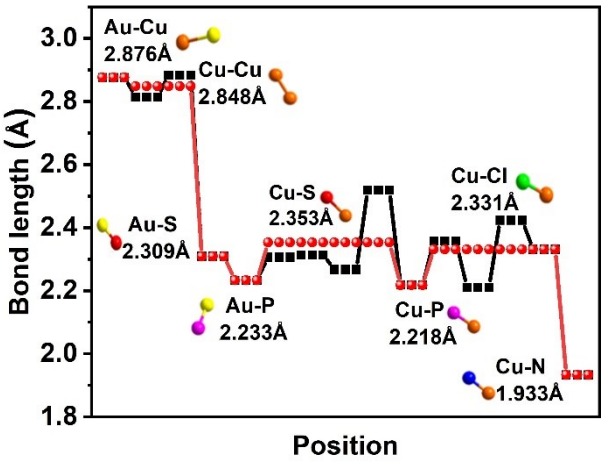


**Figure S11**. Comparison of lengths of Au-Au, Au-S, Au-P, Cu-S, Cu-P, Cu-N, and Cu-Cl of $Au_3Cu_9$. (The red spheres represent the average bond lengths, and the black squares correspond to the individual bond lengths.)

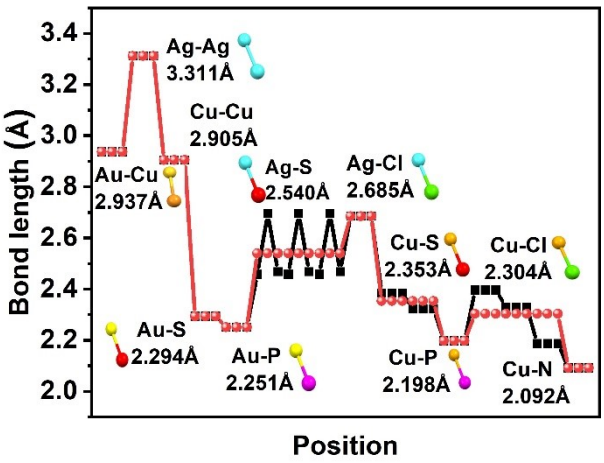


**Figure S12**. Comparison of lengths of Au-Cu, Ag-Ag, Cu-Cu, Au-S, Au-P, Ag-S, Ag-Cl, Cu-S, Cu-P, Cu-Cl, and Cu-N of $Au_3Ag_3Cu_6$. (The red spheres represent the average bond lengths, and the black squares correspond to the individual bond lengths.)

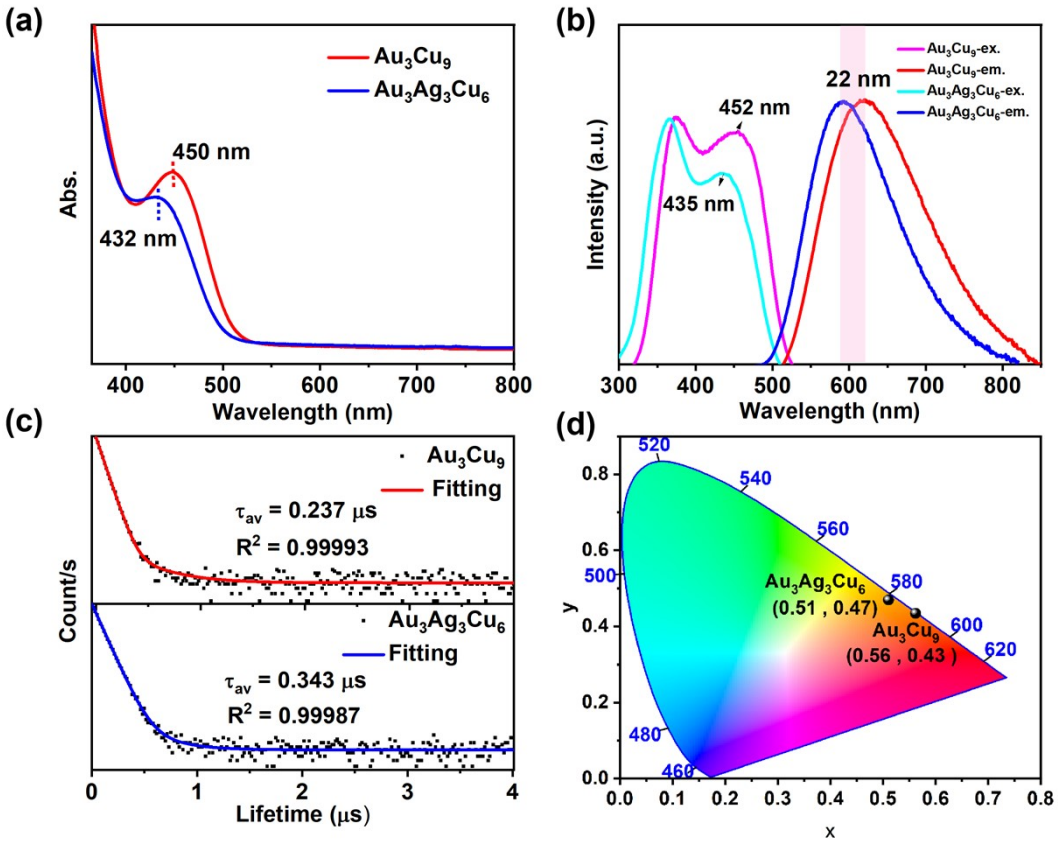


**Figure S13.** (a) Optical absorptions spectra of $Au_3Cu_9$ and $Au_3Ag_3Cu_6$ NCs in DCM. (b) Excitation and photoluminescence (PL) spectra of $Au_3Cu_9$ and $Au_3Ag_3Cu_6$ the crystal at room temperature. The dominant excitation peaks at 435 nm and 452 nm match well with their UV-vis absorption bands, while the extra peak near 370 nm is an instrumental artifact originating from xenon lamp stray light. This 370 nm signal arises from light scattering during testing and is unrelated to the intrinsic electronic transitions of the two nanoclusters. (c) Fluorescence lifetime of $Au_3Cu_9$ and $Au_3Ag_3Cu_6$ in DCM. Both decay curves were well fitted by a triple-exponential model with $\chi^2$ values close to 1.0, and the average lifetimes were further calculated to guarantee reliable fitting results. (d) CIE chromaticity coordinate diagram of the photoluminescence of the $Au_3Cu_9$ and $Au_3Ag_3Cu_6$, respectively.

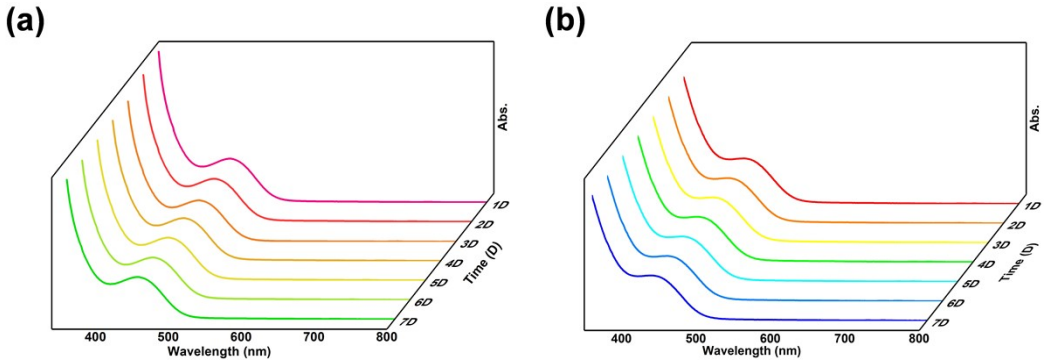


**Figure S14.** UV-vis spectra of fresh (a) $Au_3Cu_9$ and (b) $Au_3Ag_3Cu_6$ in seven days dispersed in DCM solution.

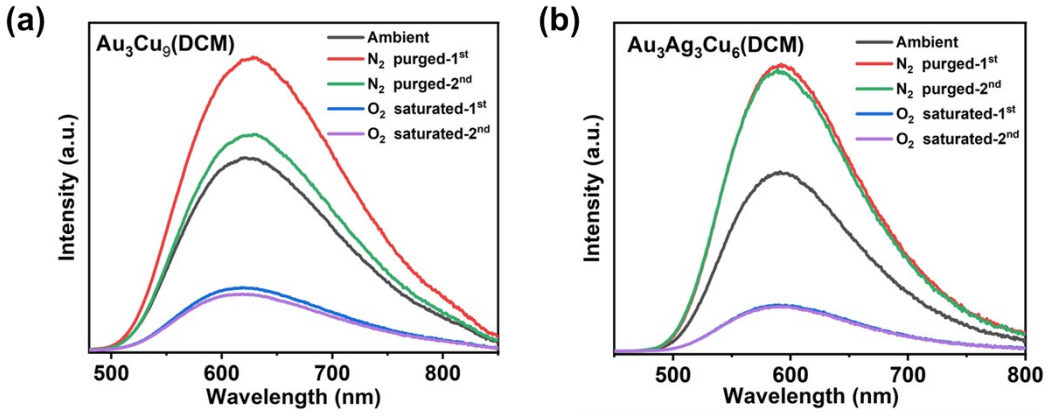


**Figure S15.** (a) $Au_3Cu_9$ and (b) $Au_3Ag_3Cu_6$ nanoclusters under ambient (black line), $N_2$-purged (red and green lines), and $O_2$-saturated conditions (blue and purple lines).

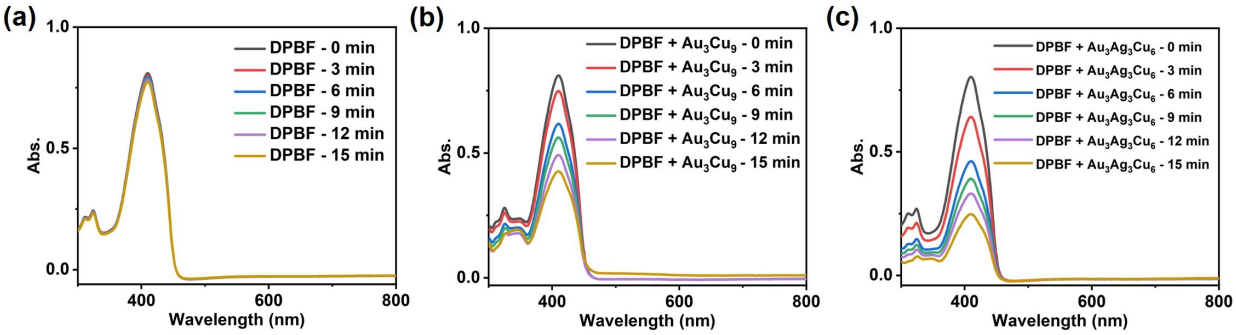


**Figure S16.** Time-dependent UV-vis absorption spectra. (a) Time-dependent UV-vis absorption spectra of the 1,3-diphenylisobenzofuran (DPBF) in EtOH solution. (b) (c) Time-dependent UV-vis absorption spectra of the DPBF in EtOH solution mixed with $Au_3Cu_9$ and $Au_3Ag_3Cu_6$.

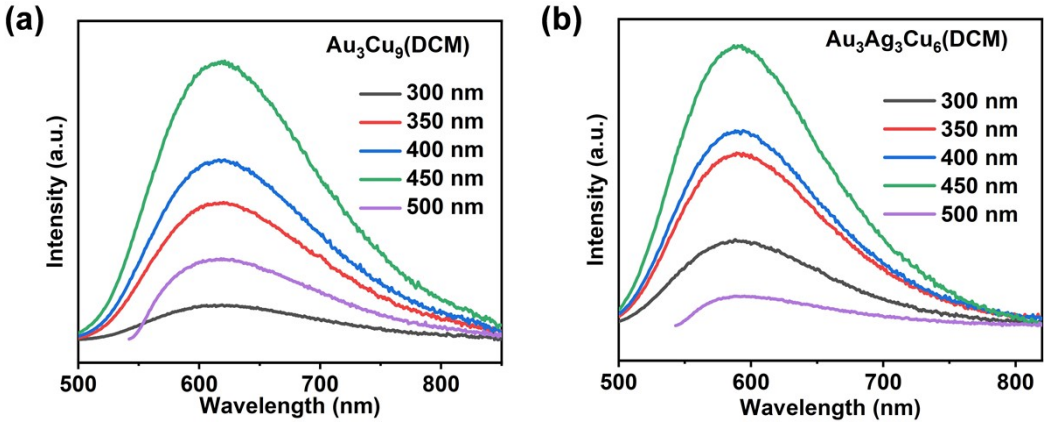


**Figure S17.** The emission spectra of (a) $Au_3Cu_9$ and (b) $Au_3Ag_3Cu_6$ in DCM solvent under different excitation wavelengths at room temperature.

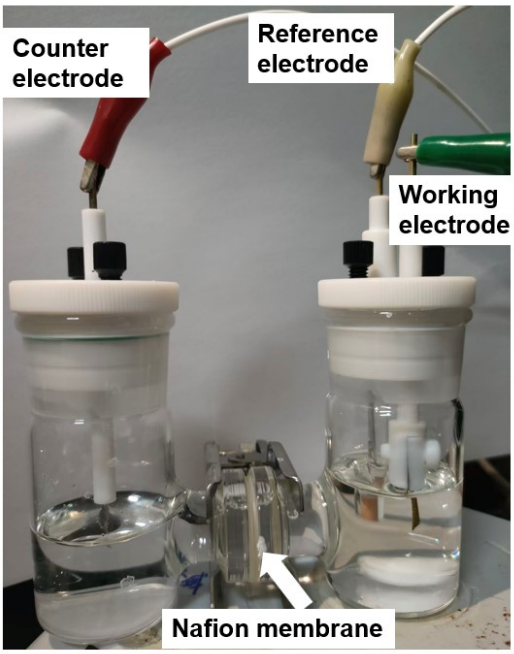


**Figure S18.** The H-cell device for $NO_3RR$.

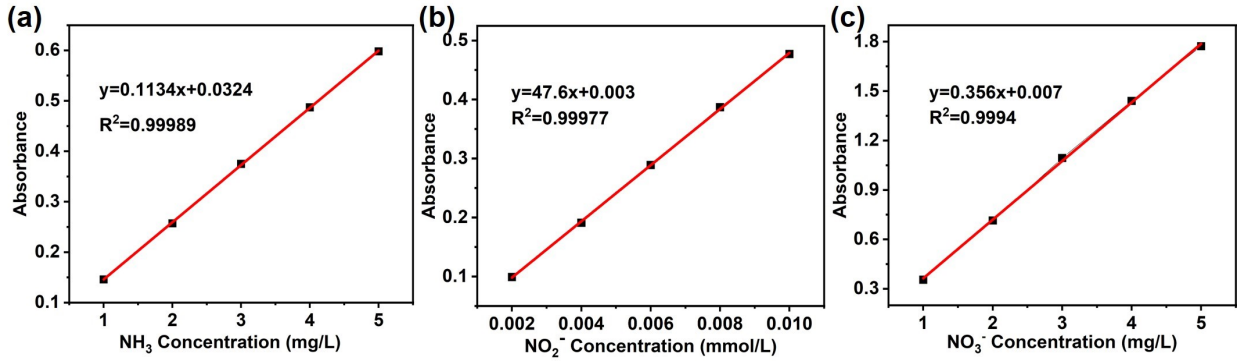


**Figure S19.** The absorbance standard curve of (a) $NH_3$, (b) $NO_2^-$, and (c) $NO_3^-$. Specifically, $NH_4^+$ was quantified via the indophenol blue method at 655 nm, $NO_2^-$ was determined using the Griess method at 540 nm, and $NO_3^-$ was analyzed by ultraviolet spectrophotometry with the dual-wavelength correction method of $A_{220}$-$2A_{275}$. The three ions adopt distinct color-developing systems and detection principles with significantly different characteristic absorption wavelengths, thereby eliminating spectral cross-interference and signal overlap.

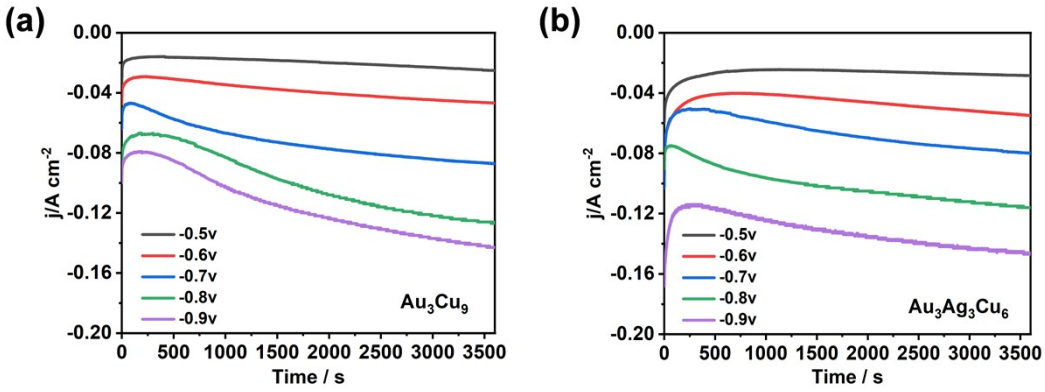


**Figure S20** i-t curves of (a) $Au_3Cu_9$ and (b) $Au_3Ag_3Cu_6$.

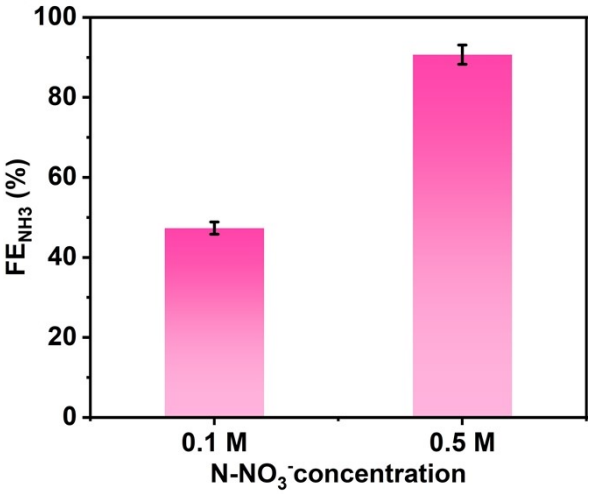


**Figure S21.** $FE_{NH3}$ of $Au_3Ag_3Cu_6$ at different $KNO_3$ concentrations.

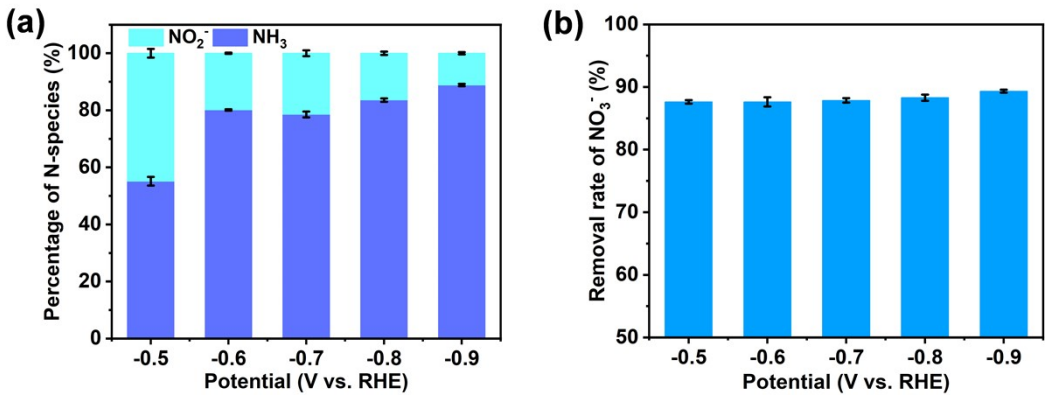


**Figure S22.** (a) The selectivity of $NH_3$ and $NO_2^-$ for $Au_3Ag_3Cu_6$, and (b) the $NO_3^-$ removal rate, both plotted as a function of applied potential from -0.5 V to -0.9 V.

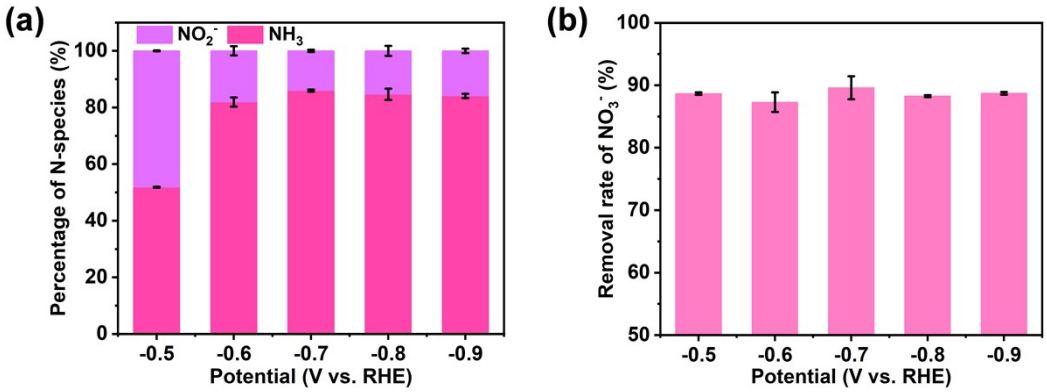


**Figure S23.** (a) The selectivity of $NH_3$ and $NO_2^-$ for $Au_3Cu_9$, and (b) the $NO_3^-$ removal rate, both plotted as a function of applied potential from -0.5 V to -0.9 V.

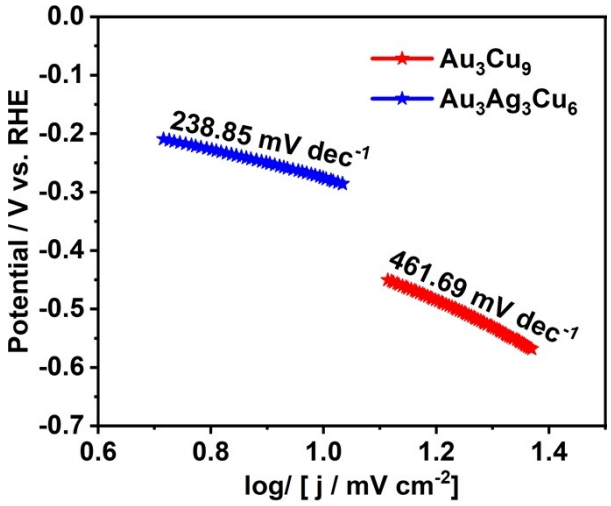


**Figure S24.** Tafel slope curves of $Au_3Cu_9$ and $Au_3Ag_3Cu_6$.

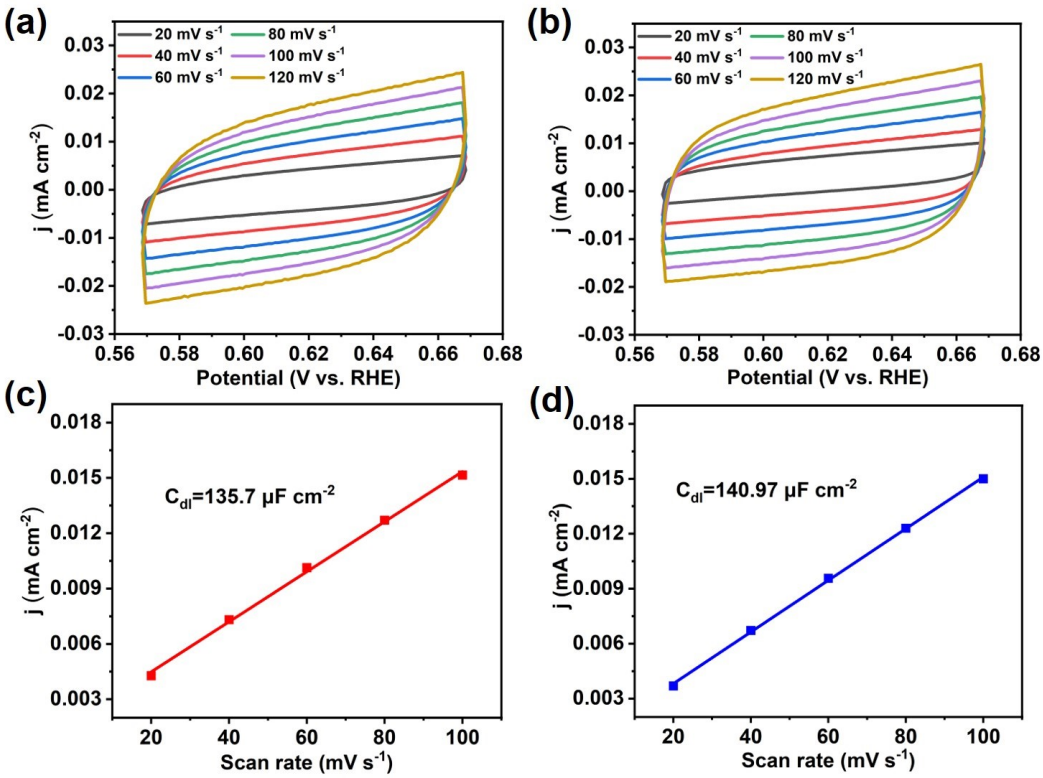


**Figure S25.** Cyclic voltammograms of (a) $Au_3Cu_9$ and (b) $Au_3Ag_3Cu_6$ in the region of 0.56 V- 0.68 V in 0.5 M $K_2SO_4$ containing 0.5 M $NO_3^-$ at various scan rates, the plots of current density as a function of scan rate derived from cyclic voltammograms of (c) $Au_3Cu_9$ and (d) $Au_3Ag_3Cu_6$.

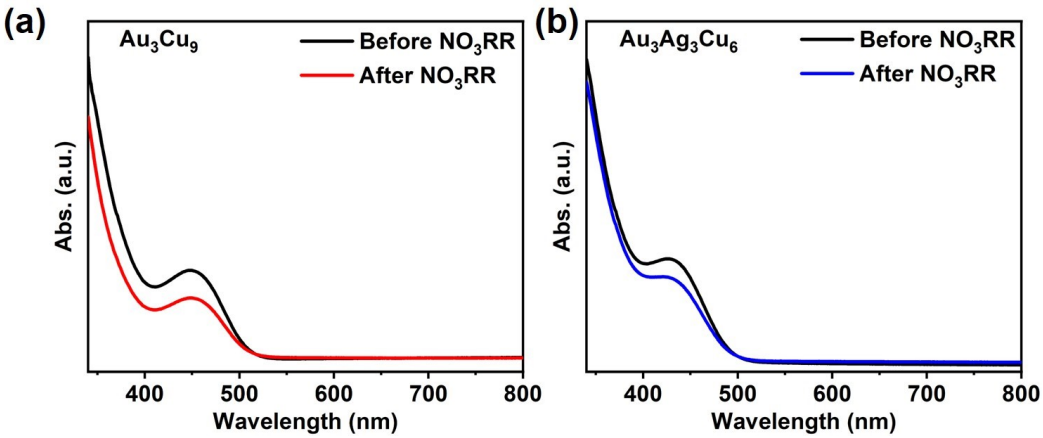


**Figure S26.** The absorbance spectra of (a) $Au_3Cu_9$ and (b) $Au_3Ag_3Cu_6$ before and after the $NO_3RR$.

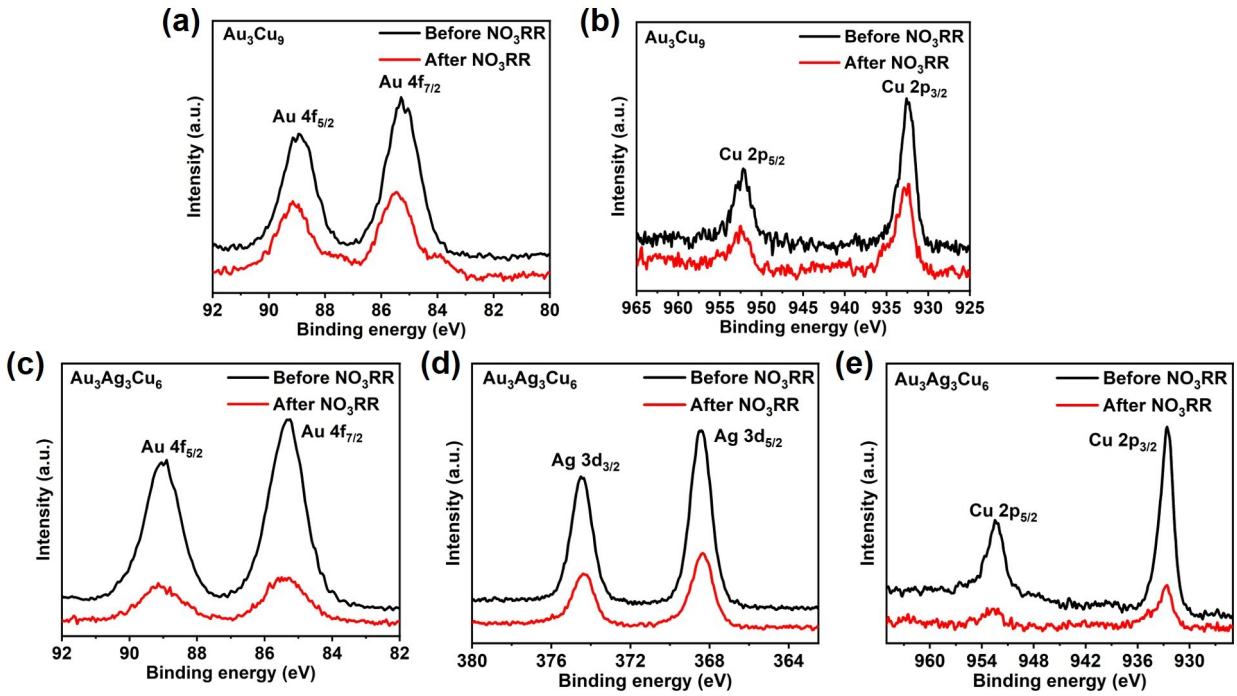


**Figure S27.** The XPS date of (a,b) $Au_3Cu_9$ and (c-e) $Au_3Ag_3Cu_6$ before and after the $NO_3RR$.

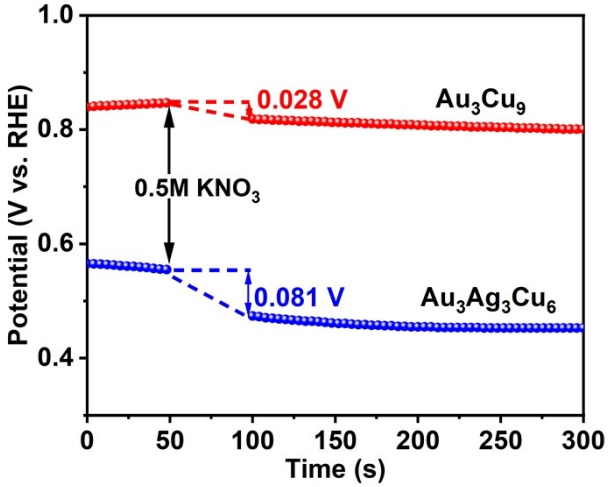


**Figure S28.** The OCP of $Au_3Cu_9$ and $Au_3Ag_3Cu_6$ in 0.5 M $K_2SO_4$ electrolyte before and after $KNO_3$ was injected.

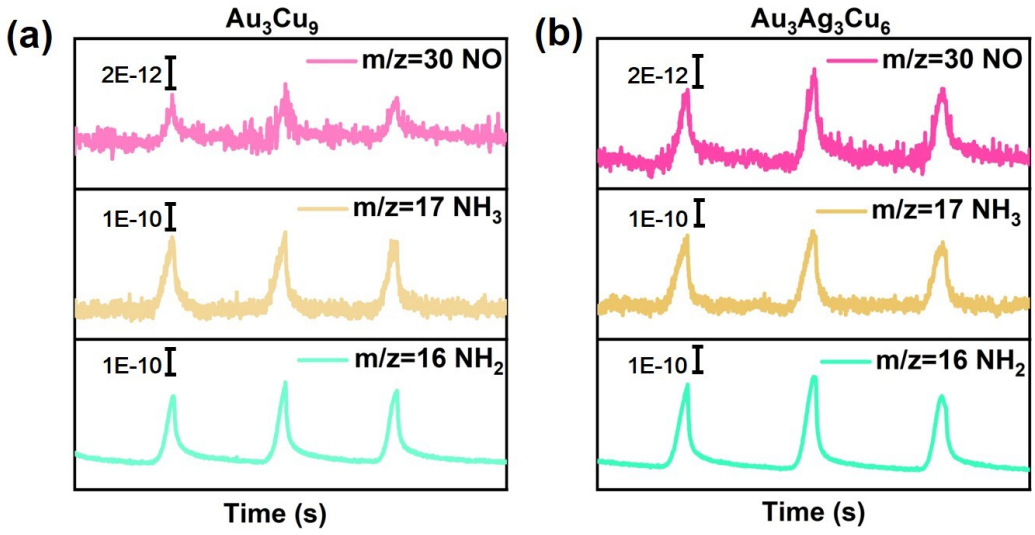


**Figure S29.** Online DEMS measurement of (a) $Au_3Cu_9$ and (b) $Au_3Ag_3Cu_6$.

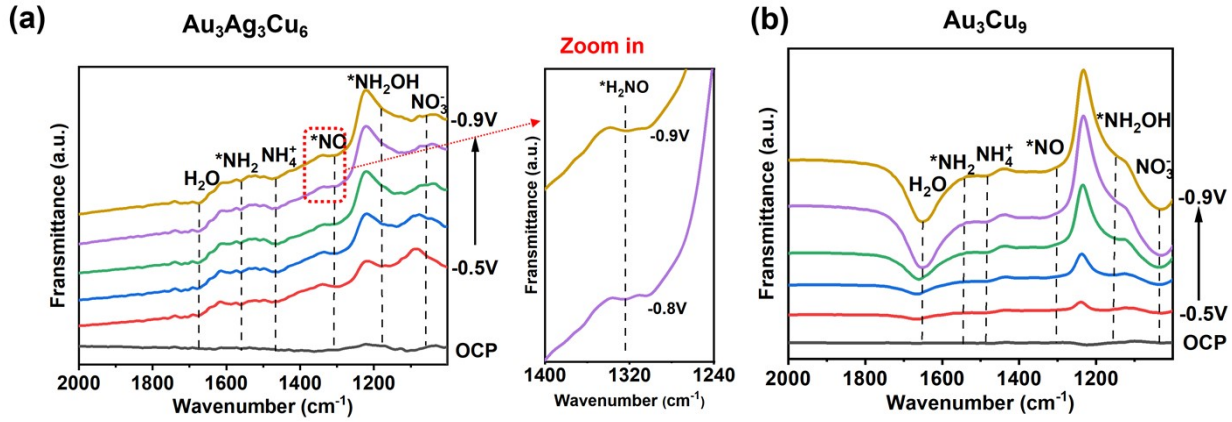


**Figure S30.** In situ FTIR spectra of (a) $Au_3Ag_3Cu_6$ and (b) $Au_3Cu_9$ from open-circuit potential to -0.9 V.

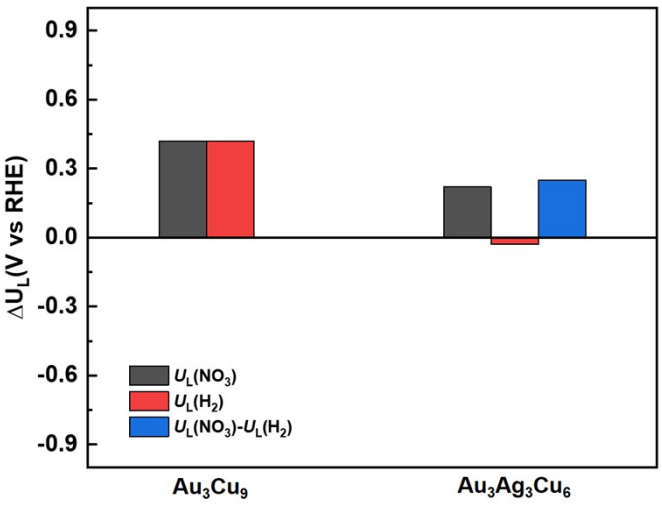


**Figure S31**. Calculated limiting potentials for $NO_3RR$, $H_2$ evolution, and their difference.

**Table S1. Crystal data and structure refinement for $Au_3Cu_9$ nanocluster**

| $Au_3Cu_9(SR)_6(dpppy)_3Cl_5$ | |
|---|---|
| Empirical formula | $C_{135}H_{87}Au_3Cl_5Cu_9F_{36}N_3P_6S_6$ |
| Formula weight | 8301.39 |
| Temperature/K | 120 |
| Crystal system | hexagonal |
| Space group | $P6_3$ |
| a/Å | 22.193(2) |
| b/Å | 22.193(2) |
| c/Å | 21.1562(18) |
| α/° | 90 |
| β/° | 90 |
| γ/° | 120 |
| Volume/Å$^3$ | 9023.8(19) |
| Z | 1 |
| Radiation | CuKα (λ = 1.54186) |
| 2θ range for data collection/° | 6.214 to 139.872 |
| Index ranges | $-26 \le h \le 15$, $-19 \le k \le 25$, $-25 \le l \le 19$ |
| Reflections collected | 29662 |
| Independent reflections | 9692 [$R_{int}$ = 0.0712, $R_{sigma}$ = 0.0625] |
| Data/restraints/parameters | 9692/1745/540 |
| Goodness-of-fit on $F^2$ | 1.047 |
| Final R indexes [I>=2σ (I)] | $R_1$ = 0.1008, $wR_2$ = 0.2715 |
| Final R indexes [all data] | $R_1$ = 0.1106, $wR_2$ = 0.2796 |
| Largest diff. peak/hole / e Å$^{-3}$ | 1.20/-1.94 |

**Table S2. Crystal data and structure refinement for $Au_3Ag_3Cu_6$ nanocluster**

| $Au_3Ag_3Cu_6(SR)_6(dpppy)_3Cl_5$ | |
|---|---|
| Empirical formula | $C_{135}H_{87}Ag_3Au_3Cl_5Cu_6F_{36}N_3P_6S_6$ |
| Formula weight | 4286.29 |
| Temperature/K | 120 |
| Crystal system | hexagonal |
| Space group | $P6_3$ |
| a/Å | 22.413(4) |
| b/Å | 22.413(4) |
| c/Å | 21.354(4) |
| α/° | 90 |
| β/° | 90 |
| γ/° | 120 |
| Volume/Å$^3$ | 9290(4) |
| Z | 2 |
| Radiation | CuKα (λ = 1.54186) |
| 2θ range for data collection/° | 6.154 to 140.914 |
| Index ranges | $-27 \leq h \leq 18$, $-25 \leq k \leq 25$, $-25 \leq l \leq 22$ |
| Reflections collected | 32689 |
| Independent reflections | 10694 [$R_{int}$ = 0.0667, $R_{sigma}$ = 0.0523] |
| Data/restraints/parameters | 10694/1686/527 |
| Goodness-of-fit on $F^2$ | 0.969 |
| Final R indexes [I>=2σ (I)] | $R_1$ = 0.0735, $wR_2$ = 0.1996 |
| Final R indexes [all data] | $R_1$ = 0.0874, $wR_2$ = 0.2097 |
| Largest diff. peak/hole / e Å$^{-3}$ | 1.36/-0.96 |

## References


1. F. Neese, *WIREs Computational Molecular Science*, 2012, **2**, 73-78.
2. F. Neese, *WIREs Computational Molecular Science*, 2018, **8**, e1327.
3. C. Adamo and V. Barone, *J. Chem. Phys.*, 1999, **110**, 6158-6170.
4. F. Weigend and R. Ahlrichs, *Physical Chemistry Chemical Physics*, 2005, **7**, 3297-3305.
5. in *Fundamental Concepts in Heterogeneous Catalysis*, 2014, 85-194.
6. D. Kim, C. Xie, N. Becknell, Y. Yu, M. Karamad, K. Chan, E. J. Crumlin, J. K. Nørskov and P. Yang, *J. Am. Chem. Soc.*, 2017, **139**, 8329-8336.
7. J. Suh, H. Choi, Y. Kong and J. Oh, *Adv. Funct. Mater.*, 2024, **34**, 2407525.
8. J.-H. Huang, H. Zhang, Z.-Y. Wang, J.-H. Hu, J. Li, J. Cai and S.-Q. Zang, *J. Am. Chem. Soc.*, 2025, **147**, 16593−16601.
9. L. Qin, F. Sun, Z. Gong, G. Ma, Y. Chen, Q. Tang, L. Qiao, R. Wang, Z.-Q. Liu and Z. Tang, *ACS Nano*, 2023, **17**, 12747−12758.